Framework for 3D histologic reconstruction and fusion with *in vivo* MRI: Preliminary results of characterizing pulmonary inflammation in a mouse model

Mirabela Rusu[a)]
Department of Biomedical Engineering, Case Western Reserve University, Cleveland, Ohio 44106

Thea Golden
Department of Pharmacology and Toxicology, Rutgers University, Piscataway, New Jersey 08854

Haibo Wang
Department of Biomedical Engineering, Case Western Reserve University, Cleveland, Ohio 44106

Andrew Gow
Department of Pharmacology and Toxicology, Rutgers University, Piscataway, New Jersey 08854

Anant Madabhushi
Department of Biomedical Engineering, Case Western Reserve University, Cleveland, Ohio 44106

Purpose: Pulmonary inflammation is associated with a variety of diseases. Assessing pulmonary inflammation on *in vivo* imaging may facilitate the early detection and treatment of lung diseases. Although routinely used in thoracic imaging, computed tomography has thus far not been compellingly shown to characterize inflammation *in vivo*. Alternatively, magnetic resonance imaging (MRI) is a nonionizing radiation technique to better visualize and characterize pulmonary tissue. Prior to routine adoption of MRI for early characterization of inflammation in humans, a rigorous and quantitative characterization of the utility of MRI to identify inflammation is required. Such characterization may be achieved by considering *ex vivo* histology as the ground truth, since it enables the definitive spatial assessment of inflammation. In this study, the authors introduce a novel framework to integrate 2D histology, *ex vivo* and *in vivo* imaging to enable the mapping of the extent of disease from *ex vivo* histology onto *in vivo* imaging, with the goal of facilitating computerized feature analysis and interrogation of disease appearance on *in vivo* imaging. The authors' framework was evaluated in a preclinical preliminary study aimed to identify computer extracted features on *in vivo* MRI associated with chronic pulmonary inflammation.
Methods: The authors' image analytics framework first involves reconstructing the histologic volume in 3D from individual histology slices. Second, the authors map the disease ground truth onto *in vivo* MRI via coregistration with 3D histology using the *ex vivo* lung MRI as a conduit. Finally, computerized feature analysis of the disease extent is performed to identify candidate *in vivo* imaging signatures of disease presence and extent.
Results: The authors evaluated the framework by assessing the quality of the 3D histology reconstruction and the histology—MRI fusion, in the context of an initial use case involving characterization of chronic inflammation in a mouse model. The authors' evaluation considered three mice, two with an inflammation phenotype and one control. The authors' iterative 3D histology reconstruction yielded a 70.1% ± 2.7% overlap with the *ex vivo* MRI volume. Across a total of 17 anatomic landmarks manually delineated at the division of airways, the target registration error between the *ex vivo* MRI and 3D histology reconstruction was 0.85 ± 0.44 mm, suggesting that a good alignment of the *ex vivo* 3D histology and *ex vivo* MRI had been achieved. The 3D histology-*in vivo* MRI coregistered volumes resulted in an overlap of 73.7% ± 0.9%. Preliminary computerized feature analysis was performed on an additional four control mice, for a total of seven mice considered in this study. Gabor texture filters appeared to best capture differences between the inflamed and noninflamed regions on MRI.
Conclusions: The authors' 3D histology reconstruction and multimodal registration framework were successfully employed to reconstruct the histology volume of the lung and fuse it with *in vivo* MRI to create a ground truth map for inflammation on *in vivo* MRI. The analytic platform presented here lays the framework for a rigorous validation of the identified imaging features for chronic lung inflammation on MRI in a large prospective cohort. © *2015 American Association of Physicists in Medicine.* [http://dx.doi.org/10.1118/1.4923161]

1. INTRODUCTION

Pulmonary inflammation is a common condition associated with a variety of lung diseases such as asthma or chronic obstructive pulmonary disorder.[1] Manifestations of inflammation include hypertrophy of airway epithelial cells, infiltration and activation of leukocytes, and structural changes to the architecture of the lung.[2,3] The quantitative characterization of pulmonary inflammation on *in vivo* imaging holds the potential to facilitate improved and early characterization of lung diseases, as well as the investigation of anti-inflammatory drugs.[4]

Recent studies have investigated the ability of *in vivo* imaging, both computed tomography (CT)[5–7] and magnetic resonance imaging (MRI),[8–11] to identify pulmonary inflammation in preclinical models. These studies suggest that *in vivo* imaging may enable characterization of pulmonary inflammation. MRI is of particular interest in this regard as it is a nonradiation modality with a potentially better ability to image pulmonary soft tissue compared to CT.[8,9,11–14] There is however a need for computerized decision support and feature analysis tools to define and evaluate quantitative imaging signatures for pulmonary inflammation on *in vivo* MRI.

Currently, in most instances, the only way to definitively ascertain the presence and spatial extent of diseases is via pathologic examination of stained histology slices (Fig. 1). While surgically excised lung histopathology could serve not only for defining the precise extent and presence of disease, it could also serve as a conduit to map the extent of disease onto the corresponding *in vivo* imaging via coregistration. Such accurate mapping of disease extent on *in vivo* imaging paves the way for a rigorous comparison of imaging appearance of disease and normal regions. Furthermore, when image intensities alone are unable to discriminate disease from other confounding tissue regions, computerized feature analysis methods such as textural analysis could help prize out subtle cues to distinguish the similar appearing tissue regions.[15–18]

In this work, we introduce a novel analytic framework to facilitate imaging signature discovery for disease. Our framework was evaluated in the context of initial MRI based characterization of chronic inflammation in a mouse model. Specifically, the framework is comprised of three modules. First, the histology specimen is digitally reconstructed in 3D in order to facilitate its fusion with *in vivo* MRI. Such reconstruction is required as correspondences between lung histology and *in vivo* MRI slices may not be ascertainable due to different image viewing and histology cutting planes.
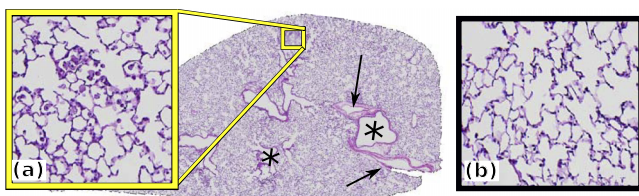

FIG. 1. Lung hematoxylin and eosin (H&E) stained slice showing regions of (a) inflammation and (b) normal tissue. Airways (*) and blood vessels (→) are visible.

Second, the 3D inflammation is mapped from the 3D reconstructed histology volume onto the *in vivo* MRI by coregistration of the 3D histology volume and the *in vivo* MRI using the *ex vivo* MRI as a conduit. Finally, image-derived features are extracted from the *in vivo* MRI of two mice with a phenotype of chronic pulmonary inflammation and the normal lung of five control mice. A comparison is performed between inflamed regions mapped from histology in two mice with an inflammation phenotype and normal lung from five control mice. By choosing these specific phenotypes, we can evaluate our framework to distinguish inflammation on *in vivo* MRI from normal lung tissue. The 3D histological reconstruction and its fusion with MRI were qualitatively and quantitatively evaluated in three mice, the two mice with an inflammation phenotype and one control mouse, while the preliminary textural analysis was performed on the latter three mice and an additional four control mice. While we do not claim in this paper to have identified the definitive computer extracted MRI features for diagnosis of pulmonary inflammation, the presented algorithmic pipeline paves the way for future discovery of validation of imaging signatures for diseases, including inflammation.

The remainder of the paper is organized as follows. First, we discuss previous work (Sec. 2) and provide an overview of our methodology (Sec. 3). A detailed methodological description of our framework is provided in Sec. 4, while the results are presented and discussed in Sec. 5. Finally, in Sec. 6, we present concluding remarks and future directions.

2. PREVIOUS WORK

In this paper, we present a pipeline of algorithmic steps in order to facilitate discovery of *in vivo* imaging signatures for disease. Specifically, in this paper, we evaluate this framework for the problem of identifying computer extracted MRI features associated with pulmonary inflammation in mice. Since our framework involves both 3D histologic reconstruction and radiology-pathology coregistration, we discuss previous related work in the context of these two areas.

Recently, a few approaches have been presented for coregistration of *ex vivo* histology and *in vivo* imaging data. Some approaches attempted to directly map the 2D histology slices onto the *in vivo* imaging by first determining and establishing slice[19–22] or landmark correspondences.[23] Alternative approaches inspired by the actual process of histology sample preparation have also been proposed.[24] Yet, when slice correspondences between the *ex vivo* histology and *in vivo* imaging datasets do not exist or are difficult to identify, 3D reconstruction techniques may allow for creation of a 3D histology volume and enable volumetric coregistration with corresponding *in vivo* imaging.[25] Such techniques are particularly useful in preclinical studies, where finely cut histologic sections corresponding to the *in vivo* imaging may be available. Some approaches have employed one-to-one registration[26–29] of histology slices by utilizing rigid[26,27] or deformable[28,29] transforms. However, one-to-one registration of adjacent slices is prone to propagation of registration errors
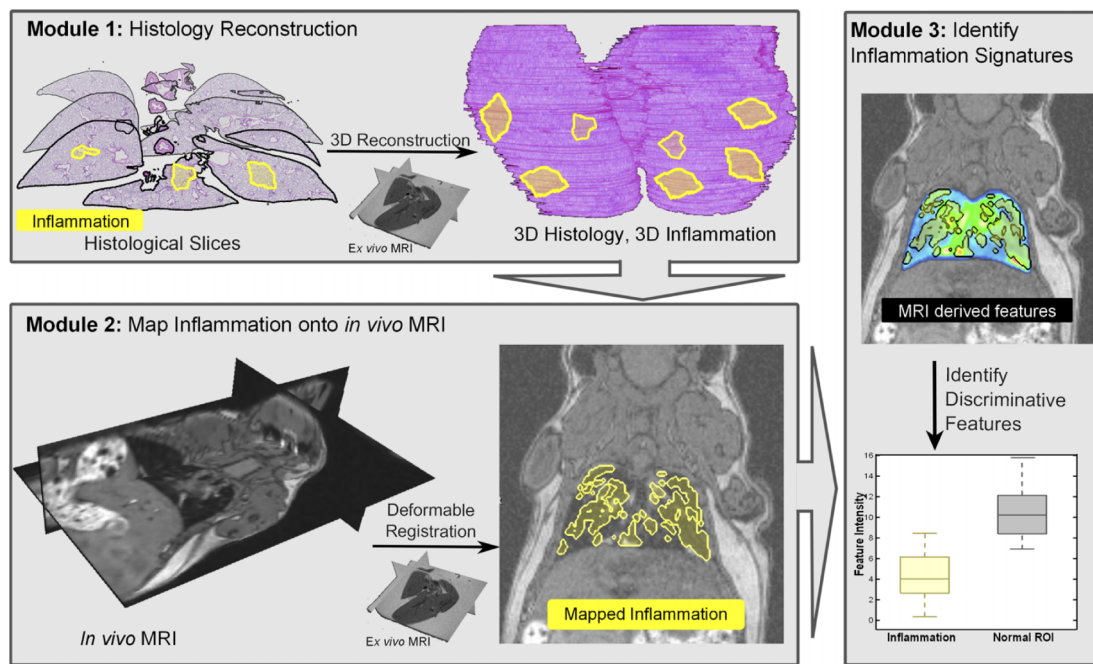
FIG. 2. Overview of our algorithmic pipeline for characterization of pulmonary inflammation. **Module 1:** 3D histology volume is reconstructed from the 2D histology sections using *ex vivo* MRI as a conduit; the reconstruction also results in the generation of a 3D map of inflammation (yellow). **Module 2:** Volumetric coregistration of 3D histology and *in vivo* MRI volumes allows for the mapping of inflammation onto *in vivo* imaging. **Module 3:** Computer extracted image features of inflammation can then be identified from the *in vivo* MRI.

between slices, resulting in a progressive shift along the Z-axis. Alternative approaches have included one-to-many[30,31] or many-to-many registration schemes[32] either using a coarse-to-fine deformable transforms[30] or natural gradients.[31] Yet these methods have not been applied in the context of a multibody registration of multiple objects relative to each other.

Once the coregistration of the histology volume and the *in vivo* MRI has been accomplished, mapping of disease extent on the *in vivo* imaging can be established. This then paves the way for application of computerized feature analysis to identify imaging features to distinguish disease presence from confounders. Such methods are needed as image intensity alone may be insufficient to capture subtle differences between normal and diseased regions.[15–18,33,34]

3. BRIEF OVERVIEW AND NOVEL CONTRIBUTIONS

The current study seeks to develop the algorithmic pipeline to pave the way for quantitative characterization of *in vivo* imaging signatures of disease. In this work, we specifically look at the use case of characterization of pulmonary inflammation on MRI in a mouse model for evaluating the framework. Figure 2 illustrates the three main modules of our framework and the novel aspects of our approach.

Module 1 (Sec. 4.B): The 3D histology volume $\mathcal{H}$ is reconstructed from the 2D histology sections using an iterative alignment scheme that progressively increases the optimization complexity from a single body registration to a multibody registration of individual lobes. This reconstruction scheme was designed to facilitate the alignment of slices between each other within the 3D volume, while simultaneously

correcting for lobe movement relative to each other during histology sample preparation. Module 1 introduces a novel multiresolution reconstruction of the 3D histology volume based on a one-to-many multibody refinement of lung lobes. This approach involves making the individual lobes "spatially aware" of each other during the registration,[35] the spatial prior information coming from the *ex vivo* MRI.

Module 2 (Sec. 4.C): The 3D histology volume $\mathcal{H}$ is registered to the *in vivo* MRI using both an affine and deformable transform with the *ex vivo* MRI serving as a conduit for the registration (similar to Module 1). The registration of the histologically reconstructed volume with the *in vivo* MRI enables the mapping of the extent of lung inflammation from the 3D histology volume onto the *in vivo* MRI. This novel registration approach limits the influence of imaging artifacts, such as elastic deformations on account of the absence of neighboring organs, as well as tissue sample preparation that causes tissue shrinkage.

Module 3 (Sec. 4.D): Textural features[36–38] are extracted from *in vivo* MRI and compared between the inflamed and not inflamed regions. The preliminary feature analysis considered in this module serves as a means of showcasing how the presented framework can enable feature discovery.

4. METHODOLOGY

4.A. Data

Seven mice were included in this study: two surfactant protein D knockout (Sftpd$^{-/-}$) mice which have a demonstrated phenotype of chronic pulmonary inflammation and five C57BL/6J wild type (WT) mice (normal controls) (Table I).

TABLE I. Description of the acquisition and preparation protocols for the multimodal radiology and pathology datasets used for evaluating our analytic framework. The 3D reconstruction of the histology was performed at 0.5x, while the *in vivo* MRI was resampled to have consistent, close to isotropic voxels sizes of 250 μm^3 for feature analysis. The lungs of two Sftpd$^{-/-}$ mice and one WT mouse were fixed, carefully sliced, and had H&E staining. These histology images were utilized to assess the accuracy of the 3D histology reconstruction approach and the quality of the histology-MRI fusion. The remaining four WT mice were only used for the validation of the textural analysis module. Since the latter four mice are control animals without an inflammation phenotype, no mapping of histology onto the imaging is required and hence was not performed.

Mouse	Count	Modality	Sequence	Resolution (μm^3)	Voxels	Annotations
	2	*In vivo* MRI	$T1$ GRE	$M \times M \times 500$ $M \in \{156, 234\}$	$256 \times 256 \times N$ $N \in \{32, 34\}$	Lung, blood vessels
Sftpd$^{-/-}$	2	*Ex vivo* MRI	$T1$ GRE	$M \times M \times 500$ $M \in \{125, 156\}$	$M \times M \times N$ $M \in \{256, 512\}$ $N \in \{20, 34\}$	Lung, airways
	2	Histology		$0.75 \times 0.75 \times 110$	$M \times M \times N$ $M \in \{5000, 15\,000\}$ $N \in \{62, 74\}$	Lung, airways Blood vessels Inflammation
	1	*In vivo* MRI	$T1$ GRE	$234 \times 234 \times 500$	$256 \times 256 \times 32$	Lung
	1	*Ex vivo* MRI	$T1$ GRE	$156 \times 156 \times 500$	$256 \times 256 \times 34$	Lung, airways
WT	1	Histology		$0.75 \times 0.75 \times 110$	$M \times M \times 79$ $M \in \{5000, 15\,000\}$	Lung, airways Blood vessels
	4	*In vivo* MRI	$T1$ GRE	$M \times M \times N$ $M \in \{156, 500\}$ $N \in \{200, 500\}$	$M \times M \times N$ $M \in \{128, 256\}$ $N \in \{30, 128\}$	Lung

The mice allow us to compare image-derived features between inflamed and noninflamed regions. The lung MRI was acquired with a 1 Tesla (T) M2 High Energy Performance MRI System (Aspect Magnet Technologies Ltd.). A $T1$-weighted MR gradient recalled echo sequence was used. Imaging parameters include TE/TR = 3.5/15 ms, flip angle 30°, 0.55 mm slice thickness. MR images were taken from *in vivo* lungs of anesthetized mice, under isoflurane, gated for peak inspiration.

After the *in vivo* MRI acquisition, the mouse lung was extracted and the inflation was fixed to the same volume as the *in vivo* MRI lung with 4% paraformaldehyde and 2% sucrose. *Ex vivo* lungs were imaged using the same sequence protocol as the *in vivo* MRI (Table I). In order to use the *ex vivo* MRI as a conduit for the histology reconstruction, the *ex vivo* images were acquired after the lung was fixed (via inflation with fixative). Since the *ex vivo* scan shows an inflated lung and to facilitate the coregistration of *in vivo* and *ex vivo* MRI, we also used an inflated lung for the *in vivo* MRI acquisition. The fixed lung was then embedded in paraffin and 5 μm sections were cut with a spacing of 110 μm (Table I). These sections were stained with hematoxylin and eosin (H&E) (Fig. 1) and digitized at 10x magnification using the Olympus VS120-SL scanning microscopy system.

The specific physiologic characteristics captured by each of the acquired modalities are summarized below.

1. **Whole body 1 T *in vivo* MRI** shows the *in vivo* lung at a lower resolution, allowing for the visualization of arteries within the lung as hyperintense densities. Other organs, e.g., heart or liver, are spatially located in the proximity of the lung, resulting in its elastic compression.

2. ***Ex vivo* MRI** shows the lung at better resolution compared to the *in vivo* MRI and allows for the visualization of large bronchi (hypointense regions). The same protocol used for *in vivo* imaging was also used for *ex vivo* imaging. The *ex vivo* acquisition provides a conduit to coregister *in vivo* MRI with *ex vivo* histology as they share similar attributes.

3. ***Ex vivo* H&E stained histology slices** are obtained from the entire lung of three mice, two Sftpd$^{-/-}$ and one WT. The lungs of the remaining four WT mice did not undergo histology preparation, as they lack inflammation, and thus, they do not require histology mapping on *in vivo* imaging. The histology images have the highest resolution, allowing for the annotation of inflammation, blood vessels, and airways. Inflammation was identified as hypertrophy of airway epithelial cells and leukocyte infiltration[39] and was manually delineated by an expert with substantial expertise in lung pathology. Large airways, blood vessels, and lung lobes were identified using an automatic active contour approach,[40] parameterized to segment connected regions of interest. The results of the automated segmentation were then further manually partitioned into different anatomic classes: airways, blood vessels, or lung lobes. In spite of careful sample preparation, the histology slices may suffer from preparation artifacts, e.g., folding and shrinking. The histology slices were downsampled to a 0.5x magnification for further processing and reconstruction.

4.B. Module 1: Reconstruction of the 3D histology volume

The 3D reconstruction follows an iterative approach (Fig. 3), in which the complexity of the registration is progressively increased. See Table II for a summary of notation used in this manuscript and Secs. 4.C and 4.D.

The reconstruction involves optimization of the following scoring function for each histological slice $\mathcal{H}_i$, $i \in \{2,\ldots,N\}$, where N represents the total number of slices:

$$\psi(\mathcal{T},\mathcal{H}_i) = \psi_{\mathcal{H}}(\mathcal{T}(\mathcal{H}_i),k,k') + \tilde{w} \cdot \psi_{\mathcal{M}}(\mathcal{T},(\mathcal{H}_i),\widetilde{\mathcal{M}}_i), \qquad (1)$$

where $\mathcal{T}$ is the rigid transformation of the slice $\mathcal{H}_i$. The term $\psi_{\mathcal{H}}$ quantifies the intrinsic alignment of $\mathcal{H}_i$ to neighboring k and k' slices located either lower and, respectively, higher in the Z stack. The Z stack refers to the third dimension in the reconstructed volume $\mathcal{H}$, where the first and second dimensions are defined relative to the 2D histology slice coordinate frame. The second term, $\psi_{\mathcal{M}}$, encodes the alignment of $\mathcal{H}_i$ with the corresponding slice in the *ex vivo* MRI, $\widetilde{\mathcal{M}}_i$, while $\tilde{w}$ represents the weight of the *ex vivo* term. Module 1 has four submodules.

1. **Module 1a. One-body backward intrinsic registration** ensures that each slice $\mathcal{H}_i$ is optimized within the reconstruction, $\forall i \in \{2,\ldots,N\}$, relative to the adjacent $k = 7$, $\mathcal{H}_{i-j}$, $j \in \{1,\ldots,k\}$, $i - j > 0$ slices located lower in the Z stack (backward registration). The *ex vivo* MRI is not considered in the scoring function as it has not yet been registered relative to the 3D histology reconstruction (i.e., $\tilde{w} = 0$). Specifically, in Module 1a, Eq. (1) becomes

$$\psi(\mathcal{T},\mathcal{H}_i) = \sum_{j=1}^{k} w_j \cdot MI(\mathcal{T}(\mathcal{H}_i),\mathcal{H}_{i-j}), \qquad (2)$$
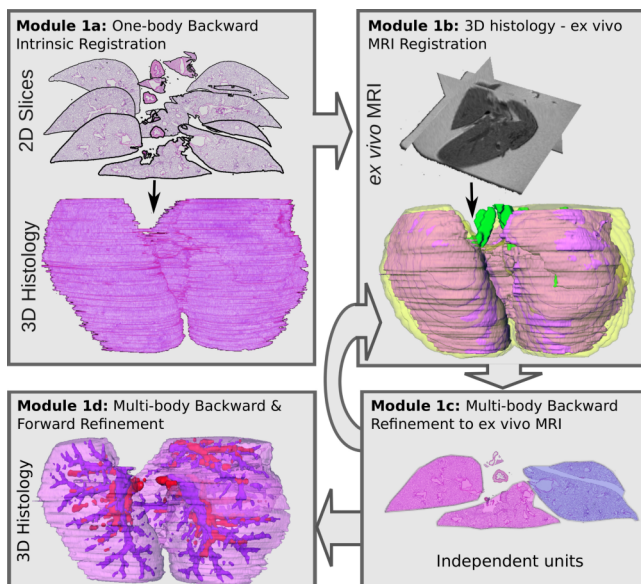

FIG. 3. Submodules of the histology reconstruction procedure (see Sec. 4.B for details).

TABLE II. Notations used in this paper.

Symbol	Definition
N	Number of histology slices
$\mathcal{H}$	3D histology volume
$\mathcal{H}_i$	Histology slice, $i \in \{1,\ldots,N\}$
$\mathcal{H}_i^m$	Unit m in $\mathcal{H}_i$
$\mathcal{A}$	Airways
$\widetilde{\mathcal{M}}$	*Ex vivo* MRI
$\widetilde{\mathcal{M}}_i$	*Ex vivo* MRI slice, $i \in \{1,\ldots,N\}$
$\mathcal{M}$	*In vivo* MRI
ψ	Optimized scoring function
$\psi_{\mathcal{H}}$	Histology scoring function
$\psi_{\mathcal{M}}$	*Ex vivo* MRI scoring function
MI	Mutual information
$\mathcal{T}$	Rigid transformation
w_j	Weight of the adjacent slice
$\tilde{w}$	Weight of *ex vivo* term

where $w_j = \exp(-(j^2/4))$ controls the influence of adjacent slices based on their proximity within the Z-stack.

2. **Module 1b. 3D histology-*ex vivo* MRI registration** ensures that the lung segmented from the *ex vivo* MRI is coregistered to the 3D histology volume, $\mathcal{H}$, using an affine transformation. A three-level pyramid registration scheme within the ITK-based package *elastix*[41] was used to optimize the normalized mutual information, employed as the scoring function.

3. **Module 1c. MultiBody backward refinement to *ex vivo* MRI** ensures that independent lobular units m are considered and their rigid transforms $\mathcal{T}^m$ are individually optimized. During histology sample preparation (fixing and staining), the five lobes may move relative to each other. The five lobes were split into two independent units, $m \in \{1,2\}$, the left and right lung, forming $\mathcal{H}_i^m$, $\forall i \in \{1,\ldots,N\}$, with their own optimized rigid transformation $\mathcal{T}_i^m$. More than two lobular units can be considered. Eq. (1) thus becomes

$$\psi(\mathcal{T}^m,\mathcal{H}_i^m) = \psi_{\mathcal{H}}(\mathcal{T}^m(\mathcal{H}_i^m),k)$$
$$+ \tilde{w} \cdot \psi_{\mathcal{M}}(\mathcal{T}(\mathcal{H}_i^m),\mathcal{H}_i^n,\widetilde{\mathcal{M}}_i), \qquad (3)$$

TABLE III. Computer extracted MRI derived features capture different types of information, e.g., quantifying the smoothness, heterogeneity, or directional patterns. These features are not intended as a comprehensive compendium of textural features, but rather as an illustration of the types of feature interrogation of the diseased regions that can be facilitated via the newly presented histologic reconstruction and radiology–pathology coregistration pipeline.

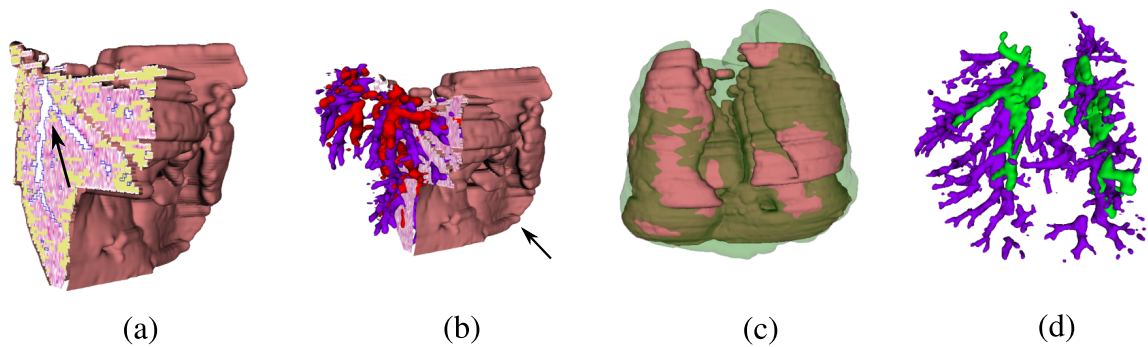| Feature category	Number of features	Captured information
First order statistics (Ref. 36)	4	Smoothness
Second order statistics (Ref. 36)	13	Edges, heterogeneity
Haralick (Ref. 37)	13	Intensity co-occurrence
Gabor filter (Ref. 38)	48	Directional linear patterns

FIG. 4. Histology volume reconstruction, $\mathcal{H}$; (a) cut through $\mathcal{H}$ shows the 3D continuity of the lung outline (brown), airways (blue outline, see arrow), and inflammation (yellow); (b) same as (a) with completely reconstructed airways (purple) and blood vessels (red); arrows point to reduced zig-zag pattern which is a qualitative indication of a good alignment; (c) overlay of $\mathcal{H}$ and *ex vivo* MRI, $\widetilde{\mathcal{M}}$ (green); (d) alignment of airways, histology (purple), *ex vivo* MRI (green).

where m, $n \in \{1,2\}$, $m \neq n$ represent independent units. $\psi_{\mathcal{H}}(\mathcal{T}(\mathcal{H}_i^m),k)$ is defined using Eq. (2) while $\psi_{\mathcal{M}}$ encodes the mutual information of the MRI slice, $\mathcal{M}_i$ and the entire histology slice, $\mathcal{H}_i$ composed of the transformed unit $\mathcal{H}_i^m$ and not transformed units $\mathcal{H}_i^n$, where $n \neq m$, $\tilde{w} > 0$.

While only the optimized unit m is considered in $\psi_{\mathcal{H}}$, all independent units, $\mathcal{H}_i^m$, are considered in the second term, $\psi_{\mathcal{M}}$. This helps to ensure that each unit is aware of the location of the other units and thus helps to limit their overlap.

4. **Module 1d. Multibody backward and forward refinement** ensures that the independent units $\mathcal{H}_i^m$ are optimized relative to the lobular units in the adjacent slices $i + j$, $j \in \{-k, k'\}$, $j \neq 0$. As opposed to Module 1c, in Module 1d, we consider the lobular units of adjacent slices located not only lower but also higher in the Z stack. Specifically, Eq. (3) becomes

$$\psi_{\mathcal{H}}(\mathcal{T}(\mathcal{H}_i^m),k,k') = \sum_{j=-k}^{k',j\neq 0} w_j \cdot MI(\mathcal{T}(\mathcal{H}_i^m),\mathcal{H}_{i+j}^m). \quad (4)$$

Module 1 iterates between the different submodules 1a–d using the following scheme. In iteration 1, the procedures defined in submodule 1a are performed. In iteration 2, the procedures defined in submodules 1b, 1c are performed. In iteration 3, the procedures defined in submodules 1b, 1c are reiterated to refine the reconstruction relative to the *ex vivo* MRI. Finally, in iteration 4, the steps in submodule 1d are employed to refine the final reconstruction. At each iteration, the transformation of each histology slice $\mathcal{H}_i, i \in \{1,\ldots,N\}$, or respective lobular unit, is refined.

Module 1 is evaluated by assessing the accuracy of the 3D histology volume reconstruction and registration with *ex vivo* MRI via the following measures.

1. The intrinsic alignment of the histology slices: $DSC_{\mathcal{H}} = 1/(N-1) \times \sum_{i=1}^{N-1} D(\mathcal{H}_i,\mathcal{H}_{i+1})$, where the dice similarity coefficient (DSC) is defined as $D(A,B) = 2|A \cap B|/(|A| + |B|)$ and $|A|$ represents the cardinality of the set A.
2. Alignment of the reconstruction, $\mathcal{H}$, with the *ex vivo* MRI: $\widetilde{DSC} = D(\mathcal{H},\widetilde{\mathcal{M}})$.

3. The alignment of L landmarks corresponding to the airway tree divisions within histology, $\mathcal{A}_{\mathcal{H},l}$, and *ex vivo* MRI, $\mathcal{A}_{\mathcal{M},l}$, $l \in \{1,\ldots,L\}$,

$$RMSD = 1/L \times \sqrt{\sum_{l=1}^{L} |\mathcal{A}_{\mathcal{H},l},\mathcal{A}_{\mathcal{M},l}|^2}. \quad (5)$$

A good reconstruction and fusion are suggested by a large DSC (max value 1) and reduced RMSD (min value: 0).

4.C. Module 2: Map disease ground truth from histology onto *in vivo* MRI volume

The linear alignment of $\mathcal{H}$ and $\mathcal{M}$ was achieved using $\widetilde{\mathcal{M}}$ as a conduit in the affine registration. To maintain the higher resolution offered by the histology, the registrations were performed using an isotropically upsampled *in vivo* MRI. $\mathcal{H}$ is warped to $\mathcal{M}$ using a B-spline based free-form deformation in a three-level pyramid registration scheme that optimizes the normalized mutual information, where the finer pyramid has a grid spacing of 4 mm. The optimized deformable transformation that warps $\mathcal{H}$ onto $\mathcal{M}$ is also applied to project the 3D inflammation ground truth on to $\mathcal{M}$, thus creating the *in vivo* ground truth for inflammation. We evaluated the registration of $\mathcal{H}$ with $\mathcal{M}$ by quantifying the alignment via $DSC = D(\mathcal{H},\mathcal{M})$.

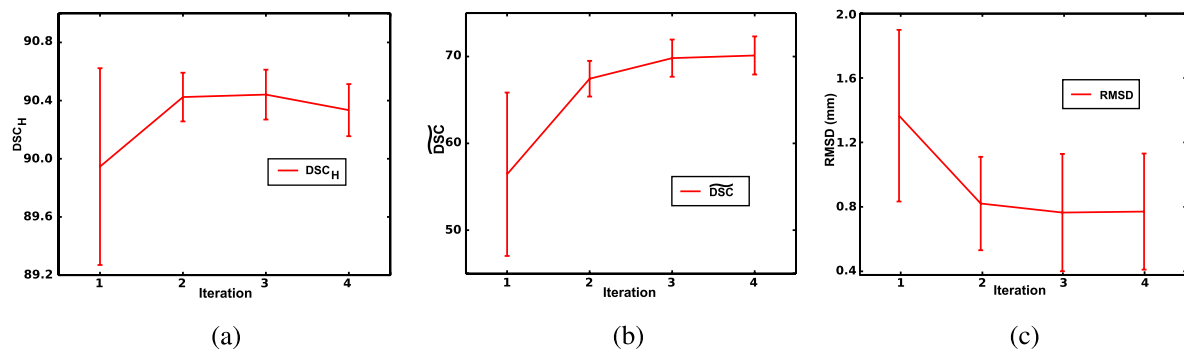FIG. 5. Reconstruction viewed from different planes, including axial, sagittal, and coronal. (Multimedia view) [URL: http://dx.doi.org/10.1118/1.4923161.1]

FIG. 6. Progression of 3D reconstruction quality per iteration shown for three mice: (a) $DSC_{\mathcal{H}}$, (b) $\widetilde{DSC}$, and (c) landmark RMSD; iteration 1 - Module 1a, iteration 2 - Modules 1b,1c; iteration 3 - Repeat Modules 1b, 1c; iteration 4 - Module 1d.

4.D. Module 3: Identify computer extracted features associated with inflammation

Following standardization of lung intensities via landmark-based histogram alignment,[42] 78 features were derived from the *in vivo* MRI in both Sftpd$^{-/-}$ and control mice after the *in vivo* MRI was resampled to a consistent 250 μm voxel size. The computer derived features extracted from $\mathcal{M}$ are summarized in Table III.

These features attempt to capture subtle subvisual differences in image intensity that may not be visibly discernible on the original MRI. For instance, Haralick features[37] capture co-occurring intensity statistics, while the Gabor filters[38] are steerable wavelets that emphasize and capture oriented gradient patterns in the image. First and second order statistics[36] are able to characterize image smoothness and identify edges.

As previously mentioned, the goal of this work was not so much to validate imaging signatures for lung inflammation, but so much as to pave the framework to facilitate feature discovery. With this in mind, we evaluated our framework with some well established image texture features to identify their association with inflammation in the lung. These features were largely drawn from classical textural operators including first and second order statistics,[36] steerable filters,[38] or Haralick features,[37] with the goal of being able to characterize the heterogeneous appearance of inflammation. Manifestations of inflammation include accumulation of foamy appearing

alveolar macrophages and of peribronchial and perivascular infiltrates in the lung.[2,3] We expect that these accumulations modify the visible smoothness of the lung, which could be captured via first and second order statistical texture features.[36] Moreover, such infiltrates may appear with similar intensity patterns at different locations within the lung, suggesting the need of Haralick features to identify such correlated patterns. The discontinuous accumulation of leukocytes may result in the creation of heterogeneous patches with borders that may be emphasized by Gabor filter features.

In order to compare the appearance profiles of inflamed and noninflamed regions and identify those textural features that are most discriminating between inflammation and noninflammation, we evaluate the difference between feature value distributions via the Bhattacharyya distance[43]

$$Bh(p,q) = -\ln\left(\sum_{b=1}^{B}(\sqrt{p_b,q_b})\right), \qquad (6)$$

where p and q are the discrete probability density function of the image derived features for the inflammation and normal regions, respectively. B represents the number of bins, while p_b and q_b are the normalized frequency of textural feature responses within each bin B.

As inflammation has a discontinuous spatial distribution, we choose to compare image derived features within inflamed regions in the Sftpd$^{-/-}$ mice and with an anatomically
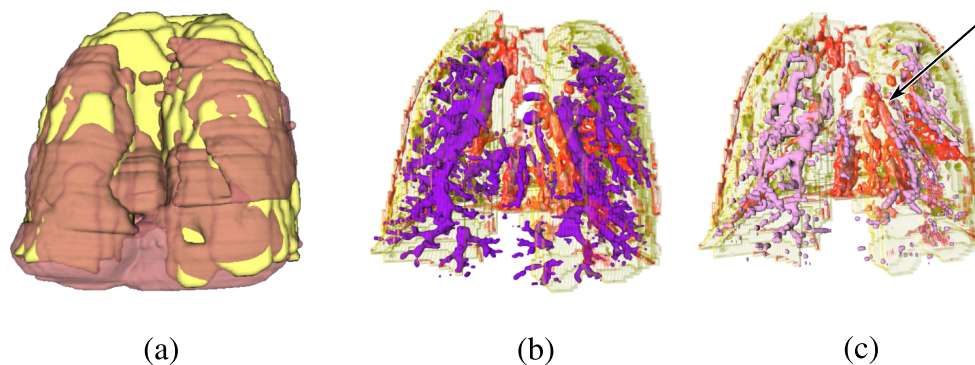

FIG. 7. Visualization of the 3D histology volume, $\mathcal{H}$ (brown), and *in vivo* MRI volume, $\mathcal{M}$ (yellow), alignment; (a) overlay of $\mathcal{H}$ and $\mathcal{M}$; (b) overlay of airways from $\mathcal{H}$ (dark purple) onto blood vessels from $\mathcal{M}$ (red). (c) Overlay of blood vessels from $\mathcal{M}$ (red) and blood vessels from $\mathcal{H}$ (pink). Arrow points to area of visually assessed close overlap.

TABLE IV. Mean and standard deviation of DSC between reconstructed histology volumes $\mathcal{H}$ and *in vivo* MRI lung volumes, $\mathcal{M}$.

Mice	Registration	
	Affine	Deformable
Sftpd$^{-/-}$	56.0 (0.7)	73.7 (0.9)
Control	62.2 (8.3)	75.9 (5.4)

TABLE V. Top five scoring features ranked according to the Bhattacharyya distance.

Feature	Parameters	Rank
Gabor	Angle: 0	1
Gabor	Angle: 2.74	2
Gabor	Angle: 0.39	3
Gabor	Angle: 0.78	4
Gabor	Angle: 2.35	5

corresponding region of interest in the control mice. The regions of inflammation were identified in the Sftpd$^{-/-}$ mice as described in Secs. 4.B and 4.C.

5. EXPERIMENTAL RESULTS AND DISCUSSION

5.A. 3D histology reconstruction

Figure 4 depicts the final results of successfully aligning the 2D H&E slices into a 3D histology volume without introducing noticeable "drift" between slices. The exterior surface of the 3D reconstruction (brown in Fig. 4) appears to be smooth, without significant zig-zag patterns visible at the edges of the reconstruction [see arrow in Fig. 4(b)].

The airways appear as continuous 3D structures [arrow in Fig. 4(a) and Fig. 5 (Multimedia view)] within the histology reconstruction [purple in Figs. 4(b) and 4(d)], suggesting minimal alignment errors between slices as illustrated in Figs. 4(a)–4(c) and assessed quantitatively by DSC$_{\mathcal{H}}$ [Fig. 6(a)]. The extracted airways appear to closely overlap in 3D between the histology and the *ex vivo* MRI lung, as illustrated in Figs. 4(d). Moreover, the high degree of reconstruction accuracy is also reflected quantitatively in the low RMSD = 0.85 ± 0.44 mm between the 17 landmark points on the 3D histology reconstruction and *ex vivo* MRI of the three mice for which the reconstruction was performed.

The reconstruction approach was evaluated for the three mice (two Sftpd$^{-/-}$ mice and one control WT) at each iteration (Fig. 6). The reconstruction $\mathcal{H}$ shows a high DSC$_{\mathcal{H}}$ following Module 1a (first iteration), suggesting that the one-to-many registration without spatial constraints is able to closely coregister the histology slices. Yet, both the $\widetilde{\text{DSC}}$ and RMSD

show their worse performance when the registration is not constrained by $\widetilde{\mathcal{M}}$.

Following the execution of Modules 1b, 1c (second iteration) in which the lobe units are simultaneously registered with constraints provided by *ex vivo* MRI, the intrinsic DSC$_{\mathcal{H}}$ and $\widetilde{\mathcal{M}}$ and landmark RMSD significantly improve, possibly reflecting the benefit of the second iteration.

In the third iteration, Modules 1b and 1c are rerun to refine the transformation of the *ex vivo* MRI and subsequently of the lobular units. Fig. 6 shows minimal improvement in DSC$_{\mathcal{H}}$, but substantial improvement of $\widetilde{\text{DSC}}$. Moreover, the decrease in RMSD suggests that the refinement of the *ex vivo* MRI transformation relative to the 3D histology reconstruction is required to further improve the reconstruction accuracy.

After Module 1d (fourth iteration), $\widetilde{\text{DSC}}$ reach their maxima, while the RMSD deviation is minimized to 0.85 ± 0.44 mm. DSC$_{\mathcal{H}}$ decreases slightly.

5.B. Fusion of 3D histology to *in vivo* MRI

Figure 7(a) shows the 3D histology volume, $\mathcal{H}$ (brown), overlaid onto *in vivo* MRI, $\mathcal{M}$ (yellow). The airway tree (purple) in Fig. 7(b) is shown relative to the blood vessels (red) extracted from $\mathcal{M}$ to depict the intertwining of the two systems. As expected, the two systems run in parallel to each other, without overlap as qualitatively seen in Fig. 7(b). Alignment accuracy is assessed qualitatively by visually investigating the blood vessel alignment, which in these figures appear to suggest close correspondences between blood vessels in $\mathcal{M}$ and $\mathcal{H}$ (pink) [see arrow in Fig. 7(c)].
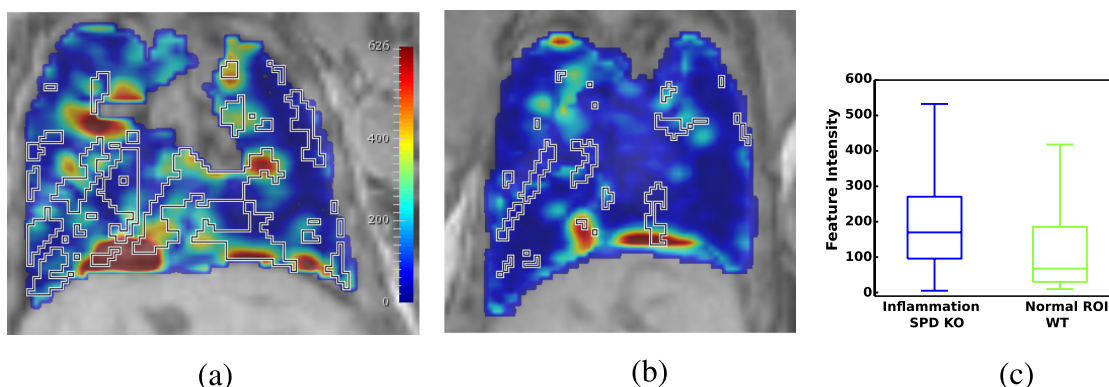

FIG. 8. Preliminary evaluation of the framework in characterizing imaging signatures of inflammation. The most discriminative feature (Gabor) is shown using the same colormap in (a) Sftpd$^{-/-}$ lung with mapped inflammation (outlined with the black and white line) from 3D histology reconstruction; (b) WT lung with volume of interest (outlined with the black and white line); (c) feature distributions show modest separation between the computer extracted features derived from the inflamed and noninflamed regions.

TABLE VI. Top three features within each feature group ranked according to the Bhattacharyya distance.

Feature	Parameters	Rank
Gabor	Angle: 0.00	1
	Angle: 2.75	2
	Angle: 0.39	3
Haralick	Energy	10
	Correlation	11
	IDM	12
First order	Median	8
	Range	13
	Mean	17
Second order	Gradient magnitude	38
	Gradient X	44
	Sobel X	56
MRI intensity		16

Table IV summarizes the quantitative evaluation via dice similarity coefficient, DSC, after each of the affine and deformable registration steps. DSC in the twoSftpd$^{-/-}$ mice is computed between $\mathcal{H}$ and $\mathcal{M}$ and not surprisingly shows an improvement in alignment following deformable registration. For the five control mice, DSC reflects the quality of registration that allows for the identification of the anatomically corresponding region of interest.

5.C. Feature characterization

Figure 8 illustrates a Gabor wavelet representation. This feature was ranked first according to the Bhatacharyya distance (Table V) reflecting the most substantial difference in distribution between the Sftpd$^{-/-}$ inflammation [Fig. 8(a)] and the corresponding volume of interest in the control mouse [Fig. 8(b)]. These differences are also reflected in the box and whiskers plot in Fig. 8(c). The statistical significance of these differences was not evaluated in this preliminary study due to the small sample size. The difference in Gabor features between inflamed and noninflamed regions appears to suggest that inflammation may influence the appearance of linear patterns within the *in vivo* MRI. Clearly, independent validation in a large cohort is needed to establish the statistical significance of these findings.

Table V shows the five-top ranked features according to the Bhattacharyya distance,[43] while Table VI shows the three-top ranked features, according to the same criterion, but within each feature class. Based on the Bhatacharyya distance criteria, the MRI intensity ranked 16 out of 79 features (Table VI), suggesting that several computer extracted features were more specific for identification of inflammation compared to the original signal intensity.

6. CONCLUDING REMARKS

We introduced a general analytic framework for 3D histologic reconstruction, multimodal fusion of radiology

and pathology in order to facilitate computer based feature interrogation of disease appearance on *in vivo* imaging. The framework enables the mapping of disease extent from the histology onto the *in vivo* imaging, creating the disease ground truth required for further feature analysis. We evaluated our framework in a preliminary study aimed at characterizing the *in vivo* MRI signature of inflammation in a preclinical mouse model. Our evaluation showed that potential candidate *in vivo* imaging computer extracted MRI features of lung inflammation may be identified using our framework.

Our methodology comprised of multiple individual modules including (1) reconstruction of 3D histology volume using *ex vivo* MRI as a conduit, (2) coregistration of the 3D histology volume with the *in vivo* MRI, and (3) textural feature comparison between diseased and normal regions. Qualitative and quantitative results suggest that the individual modules have a high degree of accuracy. Our framework yielded (1) accurate intrinsic alignment of the 2D histologic slices within the reconstruction, (2) proper alignment of the 3D histology and *ex vivo* MRI, and (3) accurate alignment of the 3D histology and *in vivo* MRI on the three mice, two Sftpd$^{-/-}$ and one control, considered in our study. Despite the high variability in *in vivo* MRI imaging parameters, resolution, and field of view, our framework was able to identify preliminary textural features that appear to be associated with pulmonary inflammation in the seven mice, two Sftpd$^{-/-}$ and five controls in our evaluation cohort.

Some challenges may influence the accuracy of the fusion of 2D histology and *in vivo* MRI lung. First, the lung is a soft tissue which is prone to major elastic deformation caused by the neighboring organs within the *in vivo* MRI. Moreover, the histology preparation causes deformation and shrinkage of the tissue. In order to account for these challenges, we used the *ex vivo* MRI as a conduit in the registration and employed a pyramid anisotropic affine registration in the 3D histology reconstruction, and a deformable registration during the histology - *in vivo* MRI fusion. The reconstruction procedure is further complicated by the lung being composed of five lobes distributed between the left and right lungs. The lobes are not attached and thus are capable of moving relative to each other during tissue excise and histological preparation. Our multibody refinement approach used during the reconstruction was implemented to overcome the possible movements of the lobes relative to each other.

The framework described in this paper was evaluated in an established mouse model of chronic pulmonary inflammation. Inflammation was identified on histology and subsequently mapped onto *in vivo* MRI for two Sftpd$^{-/-}$ mice. A similar registration approach was used to define the volume of interest in the control mice, to generate a noninflamed volume of interest that corresponds anatomically and spatially to the regions of high inflammation likelihood, as shown by the Sftpd$^{-/-}$ mice. The noninflamed volume of interest could not have been mapped from histology, since the entire volume of the lung is normal in the control animals. We anticipate that the choice of the volume of interest is not essential as the entire volume is noninflamed in the control animals, yet we made every attempt to control for anatomical and interindividual

variations by considering elastic registrations within five animals. Although, as proof-of-concept and for evaluation purposes, we performed a 3D histology reconstruction and fusion with MRI in one control animal, we considered it unnecessary for the remaining four control mice.

A total of three animals were used to evaluate the 3D histology reconstruction and its fusion with MRI. The evaluation showed good landmark and/or volumetric alignment between the 3D reconstructed histology lung and the MRI-outlined lung, indicating a proper ground truth mapping of inflammation from histology onto MRI. MRI features were extracted from a total of seven mice and were utilized to evaluate differences between inflamed and noninflamed regions. While statistical significance was not evaluated due to the small sample size, the expression patterns of some of the features warrant a subsequent in depth feature analysis. Our initial results represent preliminary data and could potentially pave the way for the use of the fusion framework in interrogation of *in vivo* imaging signatures of lung inflammation. In future work, we intend to validate the image features identified in this preliminary study on a large, independent validation cohort.

We believe our unique reconstruction and image analysis framework may be extended to include additional histological stains, molecular biomarkers, or other imaging modalities, e.g., micro-CT, to enable a comprehensive study of inflammation and other lung conditions.

[a]Author to whom correspondence should be addressed. Electronic mail: mirabela.rusu@gmail.com; Current address: GE Global Research Center, Niskayuna, New York 12309.

[1]P. K. Jeffery, "Remodeling in asthma and chronic obstructive lung disease," Am. J. Respir. Crit. Care Med. **164**, S28–S38 (2001).

[2]E. N. Atochina, M. F. Beers, S. Hawgood, F. Poulain, C. Davis, T. Fusaro, and A. J. Gow, "Surfactant protein-D, a mediator of innate lung immunity, alters the products of nitric oxide metabolism," Am. J. Respir. Cell Mol. Biol. **30**, 271–279 (2004).

[3]C. Botas, F. Poulain, J. Akiyama, C. Brown, L. Allen, J. Goerke, J. Clements, E. Carlson, A. M. Gillespie, C. Epstein, and S. Hawgood, "Altered surfactant homeostasis and alveolar type II cell morphology in mice lacking surfactant protein D," Proc. Natl. Acad. Sci. U. S. A. **95**, 11869–11874 (1998).

[4]J. Vogel-Claussen, J. Renne, J. Hinrichs, C. Schönfeld, M. Gutberlet, F. Schaumann, C. Winkler, C. Faulenbach, N. Krug, F. K. Wacker, and J. M. Hohlfeld, "Quantification of pulmonary inflammation after segmental allergen challenge using turbo-inversion recovery-magnitude magnetic resonance imaging," Am. J. Respir. Crit. Care Med. **189**, 650–657 (2014).

[5]D. L. Chen and D. P. Schuster, "Imaging pulmonary inflammation with positron emission tomography: A biomarker for drug development," Mol. Pharm. **3**, 488–495 (2006).

[6]B. N. Jobse, J. R. Johnson, T. H. Farncombe, R. Labiris, T. D. Walker, S. Goncharova, and M. Jordana, "Evaluation of allergic lung inflammation by computed tomography in a rat model in vivo," Eur. Respir. J. **33**, 1437–1447 (2009).

[7]V. Ntziachristos, "Optical imaging of molecular signatures in pulmonary inflammation," Proc. Am. Thorac. Soc. **6**, 416–418 (2009).

[8]N. Beckmann, B. Tigani, D. Ekatodramis, R. Borer, L. Mazzoni, and J. R. Fozard, "Pulmonary edema induced by allergen challenge in the rat: Noninvasive assessment by magnetic resonance imaging," Magn. Reson. Med. **45**, 88–95 (2001).

[9]B. Tigani, C. Cannet, H. Karmouty-Quintana, F.-X. Blé, S. Zurbruegg, E. Schaeublin, J. R. Fozard, and N. Beckmann, "Lung inflammation and vascular remodeling after repeated allergen challenge detected noninvasively by MRI," Am. J. Physiol. **292**, L644–L653 (2007).

[10]F.-X. Blé, C. Cannet, S. Zurbruegg, H. Karmouty-Quintana, R. Bergmann, N. Frossard, A. Trifilieff, and N. Beckmann, "Allergen-induced lung inflammation in actively sensitized mice assessed with MR imaging," Radiology **248**, 834–843 (2008).

[11]J. H. Holmes *et al.*, "Noninvasive mapping of regional response to segmental allergen challenge using magnetic resonance imaging and [F-18] fluorodeoxyglucose positron emission tomography," Magn. Reson. Med. **53**, 1243–1250 (2005).

[12]J. M. Wild, H. Marshall, M. Bock, L. R. Schad, P. M. Jakob, M. Puderbach, F. Molinari, E. J. R. Van Beek, and J. Biederer, "MRI of the lung (1/3): Methods," Insights Imaging **3**, 345–353 (2012).

[13]J. Biederer, M. Beer, W. Hirsch, J. Wild, M. Fabel, M. Puderbach, and E. J. R. Van Beek, "MRI of the lung (2/3). Why when how? Insights Imaging **3**, 355–371 (2012).

[14]J. Biederer, S. Mirsadraee, M. Beer, F. Molinari, C. Hintze, G. Bauman, M. Both, E. J. R. Van Beek, J. Wild, and M. Puderbach, "MRI of the lung (3/3)-current applications and future perspectives," Insights Imaging **3**, 373–386 (2012).

[15]S. E. Viswanath, N. B. Bloch, J. C. Chappelow, R. Toth, N. M. Rofsky, E. M. Genega, R. E. Lenkinski, and A. Madabhushi, "Central gland and peripheral zone prostate tumors have significantly different quantitative imaging signatures on 3 Tesla endorectal, in vivo T2-weighted MR imagery," J. Magn. Reson. Imaging **36**, 213–224 (2012).

[16]E. Segal, C. B. Sirlin, C. Ooi, A. S. Adler, J. Gollub, X. Chen, B. K. Chan, G. R. Matcuk, C. T. Barry, H. Y. Chang, and M. D. Kuo, "Decoding global gene expression programs in liver cancer by noninvasive imaging," Nat. Biotechnol. **25**, 675–680 (2007).

[17]O. Gevaert, J. Xu, C. D. Hoang, A. N. Leung, Y. Xu, A. Quon, D. L. Rubin, S. K. Napel, and S. Plevritis, "Non–small cell lung cancer: Identifying prognostic imaging biomarkers by leveraging public gene expression microarray data—methods and preliminary results," Radiology **264**, 387–396 (2012).

[18]P. Tiwari, J. Kurhanewicz, and A. Madabhushi, "Multi-kernel graph embedding for detection, Gleason grading of prostate cancer via MRI/MRS," Med. Image Anal. **17**, 219–235 (2013).

[19]J. Chappelow, A. Madabhushi, M. Rosen, J. Tomaszewski, and M. Feldman, "Multimodal image registration of ex vivo 4 Tesla prostate MRI with whole mount histology for cancer detection," Proc. SPIE **6512**, S1–S12 (2007).

[20]J. Chappelow, B. N. Bloch, N. Rofsky, E. Genega, R. Lenkinski, W. DeWolf, and A. Madabhushi, "Elastic registration of multimodal prostate MRI and histology via multiattribute combined mutual information," Med. Phys. **38**, 2005–2018 (2011).

[21]E. Gibson, M. Gaed, J. A. Gómez, M. Moussa, S. Pautler, J. L. Chin, C. Crukley, G. S. Bauman, A. Fenster, and A. D. Ward, "3D prostate histology image reconstruction: Quantifying the impact of tissue deformation and histology section location," J. Pathol. Inf. **4**, 31 (2013).

[22]G. Nir, R. S. Sahebjavaher, P. Kozlowski, S. D. Chang, E. Jones, L. L. Goldenberg, and S. E. Salcudean, "Registration of whole-mount histology and volumetric imaging of the prostate using particle filtering," IEEE Trans. Med. Imaging **33**, 1601–1613 (2014).

[23]C. Orczyk, H. Rusinek, A. B. Rosenkrantz, A. Mikheev, F-M. Deng, J. Melamed, and S. S. Taneja, "Preliminary experience with a novel method of three-dimensional co-registration of prostate cancer digital histology and in vivo multiparametric MRI," Clin. Radiol. **68**, e652–e658 (2013).

[24]B. Turkbey, H. Mani, V. Shah, A. R. Rastinehad, M. Bernardo, T. Pohida, Y. Pang, D. Daar, C. Benjamin, Y. L. McKinney, H. Trivedi, C. Chua, G. Bratslavsky, J. H. Shih, W. M. Linehan, M. J. Merino, P. L. Choyke, and P. A. Pinto, "Multiparametric 3 T prostate magnetic resonance imaging to detect cancer: Histopathological correlation using prostatectomy specimens processed in customized magnetic resonance imaging based molds," J. Urol. **186**, 1818–1824 (2011).

[25]H. Park, M. R. Piert, A. Khan, R. Shah, H. Hussain, J. Siddiqui, and C. R. Meyer, "Registration methodology for histological sections and in-vivo imaging of human prostate," Acad. Radiol. **15**, 1027–1039 (2008).

[26]S. Ourselin, A. Roche, X. Subsol, G. Pennec, and N. Ayache, "Reconstructing a 3D structure from serial histological sections," Image Vision Comput. **19**, 25–31 (2001).

[27]A. Cifor, T. Pridmore, and A. Pitiot, "Smooth 3-D reconstruction for 2-D histological images," in *Information Processing in Medical Imaging* (Springer, Berlin Heidelberg, 2009), pp. 350–361.

[28]L. Alic, J. C. Haeck, K. Bol, S. Klein, S. T. van Tiel, P. A. Wielepolski, M. de Jong, W. J. Niessen, M. Bernsen, and J. F. Veenland, "Facilitating tumor functional assessment by spatially relating 3D tumor histology and in vivo MRI: Image registration approach," PLoS One **6**, e22835 (2011).

[29]J. Lotz, J. Berger, B. Müller, K. Breuhahn, N. Grabe, S. Heldmann, B. Homeyer, A. Lahrmann, H. Laue, J. Olesch, M. Schwier, O. Sedlaczek, and A Warth, "Zooming in: High resolution 3D reconstruction of differently stained histological whole slide images," Proc. SPIE **9041**, 904104-1–904104-7 (2014).

[30]P. Yushkevich, B. Avants, L. Ng, M. Hawrylycz, P. Burstein, H. Zhang, and J. Gee, "3D mouse brain reconstruction from histology using a coarse-to-fine approach," in *Biomedical Image Registration*, Lecture Notes in Computer Science (Springer, Berlin Heidelberg, 2006), pp. 230–237.

[31]H. Wang, J. W. Suh, S. R. Das, J. B. Pluta, C. Craige, and P. A. Yushkevich, "Multi-atlas segmentation with joint label fusion," IEEE Trans. Pattern Anal. Mach. Intell. **35**, 611–623 (2013).

[32]M. Feuerstein, H. Heibel, J. Gardiazabal, N. Navab, and M. Groher, "Reconstruction of 3-D histology images by simultaneous deformable registration," in *Medical Image Computing and Computer-Assisted Intervention* (Springer, Berlin Heidelberg, 2011), pp. 582–589.

[33]S. Ginsburg, P. Tiwari, J. Kurhanewicz, and A. Madabhushi, "Variable ranking with PCA: Finding multiparametric MR imaging markers for prostate cancer diagnosis and grading," in *Prostate Cancer Imaging. Image Analysis and Image-Guided Interventions* (Springer, Berlin Heidelberg, 2011), pp. 146–157.

[34]G. Litjens, O. Debats, J. Barentsz, N. Karssemeijer, and H. Huisman, "Computer-aided detection of prostate cancer in MRI," IEEE Trans. Pattern Anal. Mach. Intell. **33**, 1083–1092 (2014).

[35]M. Rusu and S. Birmanns, "Evolutionary tabu search strategies for the simultaneous registration of multiple atomic structures in cryo-em reconstructions," J. Struct. Biol. **170**, 164–171 (2010).

[36]J. C. Russ, *Image Processing Handbook*, 4th ed. (CRC, Inc., Boca Raton, FL, 2002).

[37]R. M. Haralick, K. Shanmugan, and I. Dinstein, "Textural features for image classification," IEEE Trans. Syst. Man Cybern. **SMC-3**, 610–621 (1973).

[38]A. C. Bovik, M. Clark, and W. S. Geisler, "Multichannel texture analysis using localized spatial filters," IEEE Trans. Pattern Anal. Mach. Intell. **12**, 55–73 (1990).

[39]D. G. Rudmann, A. M. Preston, M. W. Moore, and J. M. Beck, "Susceptibility to pneumocystis carinii in mice is dependent on simultaneous deletion of ifn-gamma and type 1 and 2 tnf receptor genes," J. Immunol. **161**, 360–366 (1998).

[40]S. Lankton and A. Tannenbaum, "Localizing region-based active contours," IEEE Trans. Pattern Anal. Mach. Intell. **17**, 2029–2039 (2008).

[41]S. Klein, M. Staring, K. Murphy, M. A. Viergever, and J. P. W. Pluim, "Elastix: A toolbox for intensity-based medical image registration," IEEE Trans. Med. Imaging **29**, 196–205 (2010).

[42]A. Madabhushi and J. K. Udupa, "New methods of MR image intensity standardization via generalized scale," Med. Phys. **33**, 3426–3434 (2006).

[43]A. Bhattacharyya, "On a measure of divergence between two multinomial populations," Indian J. Stat. **7**, 401–406 (1946).